Strain-induced gauge and Rashba fields in ferroelectric Rashba lead chalcogenide PbX monolayers (X = S, Se, Te)

Paul Z. Hanakata,[1,*] A. S. Rodin,[2] Harold S. Park,[3] David K. Campbell,[1] and A. H. Castro Neto[2]

[1]*Department of Physics, Boston University, Boston, Massachusetts 02215, USA*
[2]*Centre for Advanced 2D Materials and Graphene Research Centre, National University of Singapore,*
6 Science Drive 2, Singapore 117546, Singapore
[3]*Department of Mechanical Engineering, Boston University, Boston, Massachusetts 02215, USA*

One of the exciting features of two-dimensional (2D) materials is their electronic and optical tunability through strain engineering. Previously, we found a class of 2D ferroelectric Rashba semiconductors PbX (X = S, Se, Te) with tunable spin-orbital properties. In this work, based on our previous tight-binding (TB) results, we derive an effective low-energy Hamiltonian around the symmetry points that captures the effects of strain on the electronic properties of PbX. We find that strains induce gauge fields which shift the Rashba point and modify the Rashba parameter. This effect is equivalent to the application of in-plane magnetic fields. The out-of-plane strain, which is proportional to the electric polarization, is also shown to modify the Rashba parameter. Overall, our theory connects strain and spin splitting in ferroelectric Rashba materials, which will be important to understand the strain-induced variations in local Rashba parameters that will occur in practical applications.

I. INTRODUCTION

Monolayers and heterostructures of two-dimensional (2D) materials with spin-orbit interactions offer promise for observing many novel physical effects [1–3]. In particular, it has been proposed that topological insulators or semiconductors with Rashba interactions coupled with superconductors may host Majorana fermions, which are potential building blocks for topological quantum computers [4,5].

In addition to 2D materials that exist in the hexagonal phase, such as graphene and the transition-metal dichalcogenides (TMDCs), 2D materials with square lattices have been successfully fabricated [6,7]. Recently, the Rashba effect has been observed in thin layers (6–20 nm) of lead sulfide (PbS) [7], where an external electric field is used to break the inversion symmetry. However, the spin splitting is not large. In our previous work based on density functional theory (DFT) calculations, we found that lead chalcogenide monolayers PbX (X = S, Se, Te) have a large Rashba coupling $\lambda \sim 1$ eV Å in their noncentrosymmetric buckled phase [8]. In addition, the spin texture can be switched in a nonvolatile way by applying an electric field or mechanical strain, which puts these materials into the family of ferroelectric Rashba semiconductors (FERSCs) [9,10]. This spin-switching mechanism has recently been observed experimentally in thin-film GeTe where the surface is engineered to have either an inward or outward electric polarization [11].

In reality, monolayers experience strains due to substrates, defects, and so on, where local strains may change the electronic properties of monolayers. Important examples of such effects are pseudo-Landau levels in graphene blisters [12] and band-gap shifts in biaxially strained MoS$_2$ [13]. Recently, spatial variations of Rashba coupling due to variations in local electrostatic potentials were reported in InSb [14]. To date, most theoretical studies of lead chalcogenide monolayers have been based solely on DFT calculations [15,16]. However, because DFT is limited to the simulation of small systems, typically several nanometers, it is difficult to model inhomogeneous strains over large spatial areas using DFT.

In this paper, based on our previous tight-binding (TB) model [8,17], we develop a continuum model to predict strain-induced changes in the spin and electronic properties of buckled PbX monolayers. We have also performed DFT calculations to validate our TB predictions. Due to the buckled structure of PbX, the angular dependence becomes important as the relative angle between hybrid orbitals of the top and bottom layer can change substantially [8]. We note that some studies on (nonbuckled) SnTe and PbX (X = S, Se, Te) rocksalt-type materials have incorporated strain effects in the TB, but did not include the changes in hopping parameters due to angle changes [18,19]. In contrast, our TB formulation incorporates the effects due to changes in (i) bond distance and (ii) angle between nearest neighbors as well as (iii) lattice vector deformation.

In the low-energy Hamiltonian, the biaxial (or uniaxial) strains can be described as gauge fields, which are equivalent to, by minimal coupling, the application of in-plane magnetic fields. The out-of-plane strain is directly related to the out-of-plane polarization and this also modifies the Rashba parameter. Within this framework we are able to quantify the Rashba fields in terms of the strain fields.

II. TIGHT BINDING

Lead chalcogenide PbX (X = S, Se, Te) consists of two atoms per unit cell, denoted by A and B atoms, respectively.
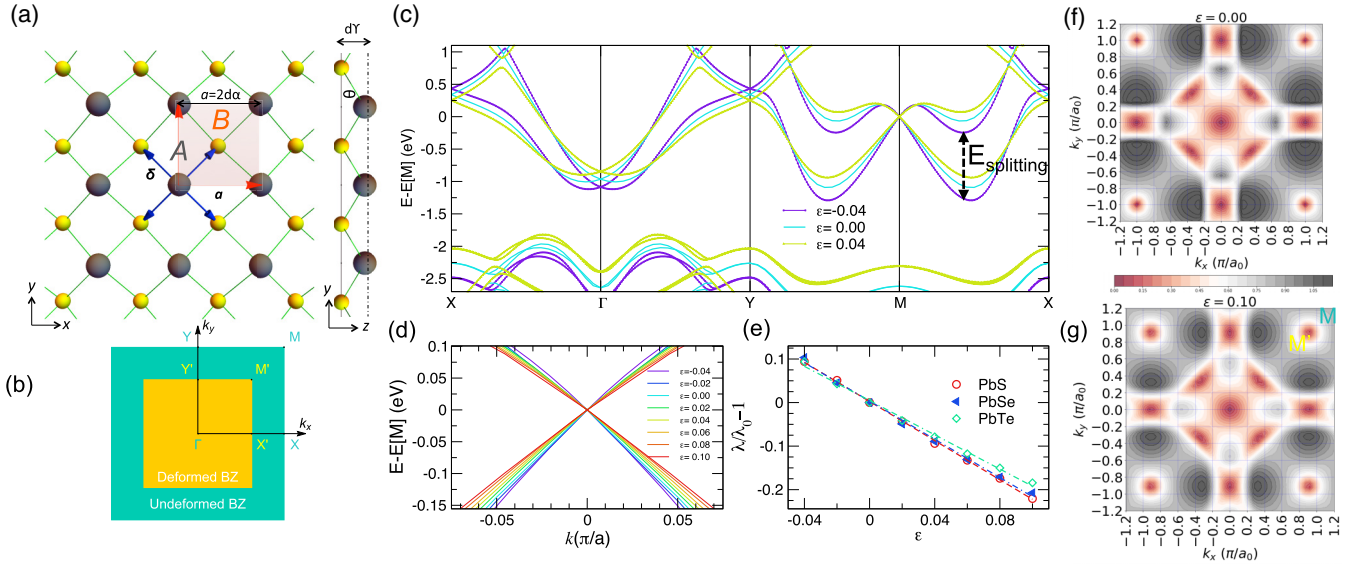
*hanakata@bu.edu

FIG. 1. (a) Schematic top and side views of a buckled AB monolayer. (b) Undeformed and deformed Brillouin zone as the monolayer is stretched in the x and y direction. (c) Representative band structures of strained PbS along symmetry points X-Γ-Y-M-X and (d) close to M. (e) Relative change in the Rashba parameters obtained from DFT calculations as a function of strain ϵ for PbS, PbSe, and PbTe. Energy spin splitting of PbS for isotropic strains of (f) $\epsilon = 0.00$ and (g) $\epsilon = 0.10$. It can be seen that the M points are originally located at $|k_{x,y}| = \pi/a_0$ and shifted closer to the center under a strain of $\epsilon = 0.10$.

Lead is a heavy atom [$Z(\text{Pb}) = 82$], and it is crucial for creating large spin-orbit interactions (SOIs). The schematic top and side views of a buckled AB lattice are shown in Fig. 1(a). $\boldsymbol{a}$ is the unit lattice vector and $\boldsymbol{\delta}_j$ is the vector connecting atom i and its j neighbor. We denote the relaxed bond length between the neighboring A and B atoms by d, the vector connecting A and B atoms in the $(0,0)$ unit cell $\boldsymbol{\delta}_1 = d(\alpha, \alpha, -\gamma)$, where $\alpha = \frac{\cos\theta}{\sqrt{2}}$, $\gamma = \sin\theta$, and θ is the buckling angle (with $\theta = 0$ corresponding to a flat lattice).

The bands near the Fermi level are mostly composed of s and p orbitals from both A and B atoms [8]. The bands near the symmetry points can be described within the TB framework including first nearest neighbors and SOI. The full derivation of the TB model can be found in our previous works [8,17], and thus we will only outline the important parts; a more detailed derivation can be found in Appendix C.

For the two-atom AB unit cell shown in Fig. 1(a), the relevant orbital basis involves $\{s^A, p_x^A, p_y^A, p_z^A, s^B, p_x^B, p_y^B, p_z^B\}$. To write down the hopping matrix, we use the Slater-Koster matrix elements for the orbitals of neighboring atoms [20]. As we include the SOI, $H_{\text{SOI}} = T_{\mathcal{X}}(\frac{L_+ \otimes s_- + L_- \otimes s_+}{2} + L_z \otimes s_z)$ (where $\mathcal{X} = A, B$), we will write our Hamiltonian in an angular momentum basis. The dimension of the total Hilbert space is 16×16 with a new basis of $|\mu\rangle \rightarrow |m\rangle|m_{\text{orb}}\rangle|s\rangle$, where $m = \{|A\rangle, |B\rangle\}$ is the sublattice degree of freedom, $m_{\text{orb}} = \{|0,0\rangle, |1,1\rangle, |1,-1\rangle, |1,0\rangle\}$ is the orbital angular momentum degree of freedom, and $s = \{(|+\rangle, |-\rangle\}$ is the spin degree of freedom.

We found a Rashba-like dispersion near the Γ and M points when the two sublattices are not equivalent [8,17]. In this paper, we develop a continuum strain model describing changes in the Rashba dispersion near the M point, and thus the Hamiltonian is expanded around the M point $\mathbf{k} = (\pi/a, \pi/a)$. Exactly at M ($q = 0$), the Hamiltonian decomposes into several uncoupled

blocks and the wave function of the conduction band is given by $|\Psi^{\pm}\rangle_{mn} = c_0|m\rangle \otimes |1, \pm 1\rangle \otimes |\mp\rangle + c_1|m\rangle \otimes |1,0\rangle \otimes |\pm\rangle \pm ic_2|n\rangle \otimes |1, \mp 1\rangle \otimes |\mp\rangle$, with c_0, c_1, and c_2 being real numbers [8,17]. The Hamiltonian for the valence band can be obtained by interchanging m and n.

Projecting the Hamiltonian onto the conduction band subspace, we obtain the effective Rashba-like Hamiltonian

$$H_{\text{eff}}^{mn} = \lambda[(\mathbf{q} \times \boldsymbol{\sigma}) \cdot \hat{z}] : \begin{pmatrix} |\Psi^+\rangle_{mn} \\ |\Psi^-\rangle_{mn} \end{pmatrix}, \tag{1}$$

where $\mathbf{q}$ is the momenta, $\boldsymbol{\sigma} = (\sigma_x, \sigma_y, \sigma_z)$, $\lambda \equiv a \sin 2\theta \Delta c_1 c_2$ is the Rashba parameter, and $\Delta = V_{pp\sigma} - V_{pp\pi}$. The coefficients c_0, c_1, c_2 can be obtained from the DFT calculations. Since we know the buckling angle θ, we can can evaluate Δ. All of the relevant (unstrained) parameters are tabulated in Appendix A.

III. STRAIN-INDUCED GAUGE FIELDS

Since the SOI is independent of lattice distortions, in this derivation we will focus on the spinless Hamiltonian and then reintroduce the spin terms. We will focus on the conduction band only, as the changes in the valence band should be similar.

Under deformation a vector connecting two points in a unit cell i can be approximated as $\boldsymbol{r}'_j - \boldsymbol{r}'_i \simeq \boldsymbol{\delta}_j + \boldsymbol{\delta}_j \cdot \nabla \boldsymbol{u}(\boldsymbol{r}_i)$, where $\boldsymbol{u} = (u_x, u_y, u_z)$ is the displacement vector, and $\nabla \boldsymbol{u} = \tilde{\boldsymbol{\epsilon}} + \tilde{\boldsymbol{\omega}}$. In this work, we focus on deformation that does not involve local rotation $\tilde{\boldsymbol{\omega}} = 0$. Similarly, between two lattice vectors, $\boldsymbol{R}'_j - \boldsymbol{R}'_i \simeq \boldsymbol{a}^i + \boldsymbol{a}^i \cdot \nabla \boldsymbol{u}(\boldsymbol{R}_i)$.

Alterations in bond distance will result in changes in the hopping energies. Since studies of lead chalcogenides under strain are very limited, we follow the Wills-Harrison's argument [21] and assume that the hopping energy $t \propto r^{-\beta_{\mu\nu}}$. Similar considerations also have been used for strained TMDCs [22–24] and phosphorene [25,26]. Note that the

hopping matrix derived from Slater-Koster has an angular dependence and these relative angles should change due to strain. Assuming the hopping matrix depends on bond distance only, the modified hopping parameter, in terms of the strain tensor $\tilde{\boldsymbol{\epsilon}}$, is $t'_{ij,\mu\nu}(\delta_{ij}) \simeq t_{ij,\mu\nu}(1 - \beta_{\mu\nu}\frac{1}{d^2}\boldsymbol{\delta}_j \cdot \tilde{\boldsymbol{\epsilon}} \cdot \boldsymbol{\delta}_j)$ [22,23]. This approximation is also the case for graphene, where the hopping modulation is approximated as $t'(\boldsymbol{\delta}_{ij}) = te^{-\beta(|\boldsymbol{\delta}_{ij}|/d-1)}$. In particular, this approximation works well for *flat* graphene under strain because the angle between p_z orbitals does not change. The angular dependence becomes more important when deformations, such as nanobubbles and kirigami patterns, create a large curvature (bending) [27,28]. In buckled lead chalcogenides, however, the relevant hopping

terms for the Rashba dispersion depend on the buckling angle even in the simple case of biaxial strains [8]. Thus we will include this angular dependence, and we will show that this is important to capture the changes in Rashba coupling with uniaxial strain.

Let the unstrained vector connecting an atom A and its neighbor be defined as $\boldsymbol{\delta}_j = (x,y,z)$ and the equilibrium distance $r = d$. Here, we show the derivation for $t_{p_x p_z}$, while the others can be found by following the same procedure. We assume $\Delta(r') = \Delta_0(\frac{r}{r'})^\beta$ and we expect $\beta \approx 3$ [21]. In Cartesian coordinates the strained hopping is given by $t_{p_x p_z}(x', y', z') = \frac{x'z'}{r'^2}\Delta_0(\frac{r}{r'})^\beta$, and by Taylor expansion we obtain

$$\delta t_{ij,p_x p_z}(x', y', z') \simeq - t_{ij,p_x p_z}(x,y,z)\Big([(2+\beta) - (r/x)^2]\frac{1}{r^2}\mathbf{x} \cdot (\mathbf{x'} - \mathbf{x}) - [2+\beta]\frac{1}{r^2}\mathbf{y} \cdot (\mathbf{y'} - \mathbf{y})$$

$$- [(2+\beta) - (r/z)^2]\frac{1}{r^2}\mathbf{z} \cdot (\mathbf{z'} - \mathbf{z})\Big). \tag{2}$$

Within the strain approximation, $\mathbf{x'} - \mathbf{x} = \hat{x} \cdot \tilde{\boldsymbol{\epsilon}} \cdot \boldsymbol{\delta}_j$. If we alter only the bond distance while keeping the angle constant, we will get the same expression as above when angular effects are assumed to be negligible.

The interlattice-spinless Hamiltonian in reciprocal space can be written as

$$H_{\text{orb}}^{\text{int}}(\mathbf{k}) = \sum_{\mu,\nu}\sum_{\langle ij\rangle}(t_{ij,\mu\nu} + \delta t_{ij,\mu\nu})e^{i\mathbf{k}\cdot\boldsymbol{\Delta}_j(1+\tilde{\boldsymbol{\epsilon}})}c_{i,\mathbf{k},\mu}^\dagger c_{j,\mathbf{k},\nu} + \text{H.c.}$$

$$= \underbrace{\sum_{\mu,\nu}\sum_{\langle i,j\rangle}t_{ij,\mu\nu}e^{i\mathbf{k}\cdot\boldsymbol{\Delta}_j}c_{i,\mathbf{k},\mu}^\dagger c_{j,\mathbf{k},\nu}}_{H_0} + \underbrace{\sum_{\mu,\nu}\sum_{\langle i,j\rangle}it_{ij,\mu\nu}\mathbf{k}\cdot\tilde{\boldsymbol{\epsilon}}\cdot\boldsymbol{\Delta}_j e^{i\mathbf{k}\cdot\boldsymbol{\Delta}_j}c_{i,\mathbf{k},\mu}^\dagger c_{j,\mathbf{k},\nu}}_{H^{(1)}} + \underbrace{\sum_{\mu,\nu}\sum_{\langle i,j\rangle}\delta t_{ij,\mu\nu}e^{i\mathbf{k}\cdot\boldsymbol{\Delta}_j}c_{i,\mathbf{k},\mu}^\dagger c_{j,\mathbf{k},\nu}}_{H^{(2)}} + \mathcal{O}(\epsilon^2),$$

$$\tag{3}$$

where $\langle ij\rangle$ is the sum over nearest-neighbor pairs and $\boldsymbol{\Delta}_j = \mathbf{R}_j - \mathbf{R}_i$. The first term H_0 is the unstrained Hamiltonian, $H^{(1)}$ is the correction due to lattice deformation, and $H^{(2)}$ is the correction from the altered hopping parameter due to changes in both the interatomic distance and angle between orbitals.

IV. HOMOGENEOUS ISOTROPIC STRAINS

We start with a simple deformation with no shear, $\tilde{\boldsymbol{\epsilon}} = \begin{pmatrix} \epsilon_{xx} & 0 & 0 \\ 0 & \epsilon_{yy} & 0 \\ 0 & 0 & \epsilon_{zz} \end{pmatrix}$. We will focus on the matrix elements that are relevant to the conduction band, such as $|A\rangle|1,0\rangle$ and $|B\rangle|1,1\rangle$. In the *angular momentum* basis, the correction from $H^{(1)}$ and $H^{(2)}$ at M is given by

$$_A\langle 1,0|H^{(1)}|1,1\rangle_B = a_0\sqrt{2}\alpha_0\Delta_0\gamma_0[\epsilon_{xx}\pi/a_0 + q_x\epsilon_{xx} - i\epsilon_{yy}\pi/a_0 - iq_y\epsilon_{yy}],$$

$$_A\langle 1,0|H^{(2)}|1,1\rangle_B = -a_0\sqrt{2}\alpha_0\gamma_0\Delta_0\alpha_0^2(2+\beta)[(\epsilon_{xx} + f_1\epsilon_{yy} + f_2\epsilon_{zz})q_x - (f_1\epsilon_{xx} + \epsilon_{yy} + f_2\epsilon_{zz})iq_y], \tag{4}$$

where $\epsilon_{ij} = \frac{1}{2}(\frac{\partial u_i}{\partial x_j} + \frac{\partial u_j}{\partial x_i} + \frac{\partial u_l}{\partial x_i}\frac{\partial u_l}{\partial x_j})$, $f_1 = 1 - \frac{1}{\alpha_0^2(2+\beta)}$, and $f_2 = \frac{\gamma_0^2}{\alpha_0^2} - \frac{1}{\alpha_0^2(2+\beta)}$. Note that $a_0, \alpha_0, \beta_0, \gamma_0, \Delta_0$ are the *unstrained* geometrical and hopping parameters. $H^{(1)}$ is independent of the z direction strains (e.g., ϵ_{xz}) because the lattice vector $\mathbf{R}$ and $\mathbf{k}$ are two dimensional. Because of the symmetry of M, we found that the first correction at M due to bond alterations is first order in ϵ *and* momentum q. In graphene, the first correction from the hopping modulation that is linear in ϵ (but not proportional to q) is not zero [29–31]. We have to include the contributions of $H^{(1)}$ up to first order in q as well because in $H^{(2)}$ (β-dependent term) we keep terms up to first order in q and ϵ.

To obtain β we will consider an isotropic strain $\epsilon \cdot 1_{3\times3}$. Notice that the change in the low-energy Hamiltonian of Eq. (1) due to $H^{(1)}$ and $H^{(2)}$ at M can be written as gauge potentials,

$$H_{\text{eff}} = -i\lambda_0\begin{pmatrix} 0 & (q_x - iq_y) + \boldsymbol{A}_1 + \boldsymbol{A}_2 \\ (q_x + iq_y) + \boldsymbol{A}_1^* + \boldsymbol{A}_2^* & 0 \end{pmatrix}, \tag{5}$$

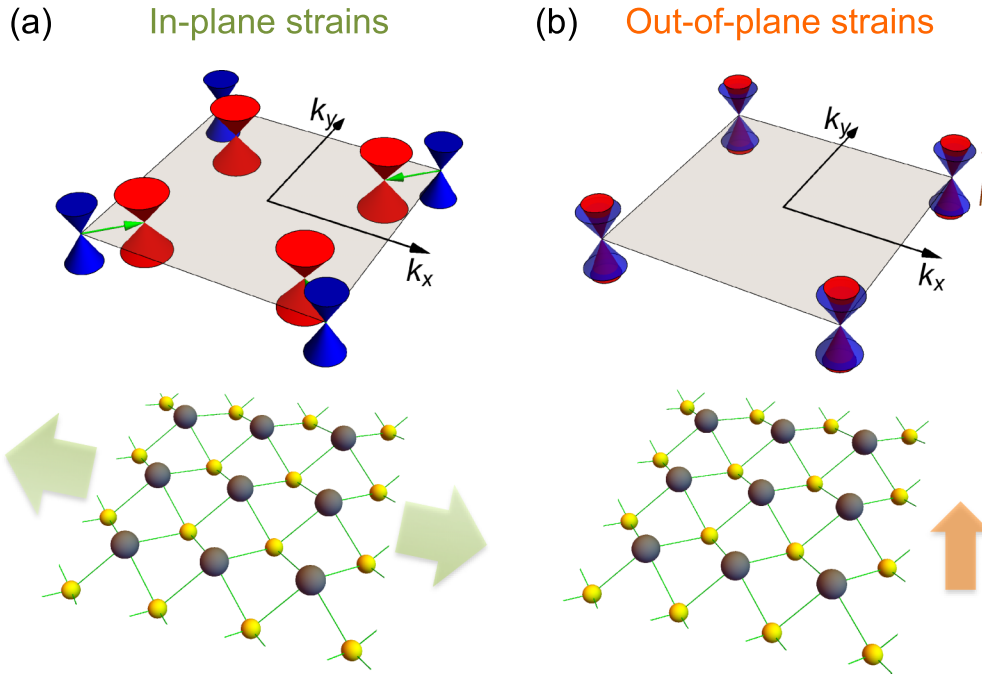## (a) In-plane strains

(b) Out-of-plane strains

FIG. 2. Schematic changes in the Rashba dispersions due to (a) in-plane strains and (b) out-of-plane strains. The linear Rashba dispersions at the M for unstrained systems are colored blue. Under positive in-plane strains, the Rashba points shift closer to Γ and the strength of the Rashba parameters decreases (smaller slope) with increasing strains. On the other hand, under out-of-plane strain, the strength of the Rashba parameters increases with increasing uniaxial out-of-plane strain while the Rashba points do not shift.

where $\boldsymbol{A}_1 = \left(\begin{smallmatrix} \epsilon\pi/a_0 + \epsilon\,q_x \\ -i\epsilon\pi/a_0 - i\epsilon\,q_y \end{smallmatrix}\right)$ and $\boldsymbol{A}_2 = -\beta\left(\begin{smallmatrix} \epsilon\,q_x \\ -i\epsilon\,q_y \end{smallmatrix}\right)$, where we have used $2\alpha_0^2 + \gamma_0^2 = 1$ to simplify $\boldsymbol{A}_1, \boldsymbol{A}_2$ and λ_0 is the unstrained Rashba parameter.

$\boldsymbol{A}_2$ and the second term of $\boldsymbol{A}_1$ are *proportional* to q. This modifies the strength of the Rashba parameter $\frac{\lambda}{\lambda_0} - 1 \simeq (1 - \beta)\epsilon$. This alteration in the Rashba term is similar to the modification of Fermi velocity in graphene [30–32].

We next present our DFT results to validate our TB predictions. Details of DFT calculations and the unstrained geometrical parameters of buckled PbS, PbSe, and PbTe can be found in Appendix A. Strains are applied to the relaxed buckled phase. In order to find the effects that come from changes in bond distance only, we deformed the monolayer in the DFT simulations by changing the bond distance while keeping the angle constant. The lattice vectors and atomic positions are not relaxed under this deformation. The Rashba parameters λ are obtained by taking the derivative of the energy dispersion in the vicinity of the M point, $|q| < 0.1\pi/a$. Under isotropic deformations, we found that λ at M decreases with increasing strain (weakening of the hopping interaction), as expected from Eq. (5), shown in Figs. 1(c)–1(e). A direct comparison between DFT results and TB with strain included allows us to extract β. By fitting DFT data points to a straight line, we obtained $\beta = 3.25, 3.20, 2.97$ for PbS, PbSe, and PbTe, respectively [Fig. 1(e)]. We see that the value of β would be different if the lattice deformation correction was not included.

As we stretch the lattice, the Brillouin zone (BZ) will shrink, and the corner of the BZ (M point) will shift as $(\frac{\pi}{a_0}, \frac{\pi}{a_0}) \rightarrow (\frac{\pi}{a_0(1+\epsilon)}, \frac{\pi}{a_0(1+\epsilon)}) \simeq (\frac{\pi}{a_0}(1-\epsilon), \frac{\pi}{a_0}(1-\epsilon))$, where a_0 is the undeformed lattice constant. For positive strains, the M point shifts towards the Γ point (relative to the undeformed

BZ), shown in Fig. 1(b). In our modified TB model, the M point is displaced due to the first term of the lattice deformation correction $\boldsymbol{A}_1$ [see Eq. (5)]. The momentum shifts due to lattice deformations are also found in graphene [33]. The changes in the Rashba dispersion and its locations due to strains are illustrated in Fig. 2.

To show the momentum shifts relative to the undeformed (reference) state, we plot the energy spin splitting at the conduction band of PbS obtained from the DFT results as a function of k_x, k_y, shown in Figs. 1(f) and 1(g). Note that momenta are in units of π/a_0. Originally, the M points are located at $|k_{x,y}| = \pi/a_0$ and are shifted closer to Γ ($|k'_{x,y}| \approx 0.9\pi/a_0$) when an isotropic strain of $\epsilon = 0.10$ is applied. The momentum shift is linear with strains $\mathbf{k} \cdot \tilde{\boldsymbol{\epsilon}}$, consistent with several previous works [31,33]. This Rashba-point shift due to strains is equivalent to applying in-plane magnetic fields $\mathbf{B}_{\text{ex}}$ to the system,

$$H = \lambda_0 \left[\left(\mathbf{q} - \frac{e\mathbf{A}_{\text{ex}}}{c} \right) \times \boldsymbol{\sigma} \right] \cdot \hat{z} + m_\perp \sigma_z B_\perp + m_\parallel \mathbf{B}_\parallel \cdot \sigma_\parallel,$$

(6)

where $m_\perp = -\mu_B(c_1^2 - 2c_2^2)$, $m_\parallel = -\mu_B c_1(\frac{c_0}{\sqrt{2}} + c_1 + c_0)$, and μ_B is the Bohr magneton. For completeness, the derivation of Eq. (6) is included in Appendix D. As an illustration, we can choose an external field of $\mathbf{A}_{\text{ex}} = (0, 0, B_x y - B_y x)$, upon which the in-plane magnetic field is given by $\mathbf{B}_{\text{ex}} = \nabla \times \mathbf{A}_{\text{ex}} = (B_x, B_y, 0)$. Since the Bohr magneton is small, in order to get a similar effect of 2% strain using magnetic fields, one has to apply external magnetic fields with an approximate strength of $|B_{\text{ex}}| \sim \frac{\sqrt{2}0.02\pi\lambda_0}{a_0 m_\parallel} \approx 600$ T [by Eqs. (5) and (6)].

V. ELECTRIC POLARIZATION AND RASHBA FIELD

Proposals have been made to change the spin texture (i.e., sign of λ) by changing the electric polarization [9,34–36]. Rinaldi *et al.* found that the spin texture in FERSC GeTe films indeed depends on the locations of the atoms on the surface, which dictate the direction of the electric polarization [11]. In DFT simulations of SnTe thin films, which have a structure similar to PbX, it also has been shown that near the vacuum one of the atomic species buckles outward while the other species buckles inward [37]. While the proportionality between the Rashba parameter and spontaneous electric polarization is well known, it will be useful to understand this mechanism in PbX from a microscopic view, where the changes in the Rashba parameters can be understood in terms of interactions between atoms and the external applied strains. We will show that our strain-dependent TB model captures how the out-of-plane strain, which is proportional to the out-of-plane polarization, modifies the Rashba fields.

By the modern theory of polarization, the electric polarization is given by [38] $\vec{\mathcal{P}} = \frac{1}{V} \sum_\tau q_\tau^{\text{ion}} \mathbf{R}_\tau - \frac{2ie}{(2\pi)^3} \sum_n^{\text{occ}} \int_{\text{BZ}} d^3\mathbf{k} e^{-i\vec{k}\cdot\mathbf{R}} \langle \Psi_{n\mathbf{k}} | \frac{\partial \Psi_{n\mathbf{k}}}{\partial \mathbf{k}} \rangle$, where q_τ is the ionic charge plus the core electrons, $\mathbf{R}_\tau$ is the position of ions, V is the unit cell volume, e is the elementary charge, n is the valence band index, $\mathbf{k}$ is the wave vector, and $\Psi_{n\mathbf{k}}$ is the electronic wave function. The first term is the contribution from core electrons and ions, and the second term is the electronic contribution defined as the adiabatic flow of current, which can be calculated from the Berry phase (BP) [38]. The spontaneous polarization is calculated by taking the difference between the polarization of the polar (buckled) state and the nonpolar (reference) state, $\Delta\vec{\mathcal{P}} = \vec{\mathcal{P}}_{\text{polar}} - \vec{\mathcal{P}}_{\text{nonpolar}}$. We estimate the thickness to be 0.5 nm in order to compare the polarizations to typical bulk ferroelectrics. Details can be found in Appendix B. In the DFT simulations we distort the ions in the z direction while keeping the in-plane lattice vectors fixed at the relaxed buckled values. We report only the spontaneous polarizations of PbS and PbSe, as PbTe is metallic [8]. A modified Berry phase calculation is needed to evaluate the polarization of ferroelectric metals [39], however, this is beyond the scope of our present study.

From the DFT results we found that the core electronic plus ionic and the electronic contribution (BP) are proportional to the distance between Pb and X ($X = $ S, Se) in the z direction (plotted in Appendix B). This gives a proportionality between $\Delta\vec{\mathcal{P}}_z$ and ϵ_{zz}, as shown in Fig. 3(a). Compressing the monolayer in the $\hat{z}$ with strain $\epsilon_{zz} < 0$ results in a decrease in λ, shown in Fig. 3(b). This is *opposite* to the case of isotropic deformation [see Fig. 1(e)]. This result is consistent with TB predictions. In the previous discussion, we found that increasing bond distance ($\epsilon > 0$) generally weakens the hopping interaction and thus decreases λ. Using relaxed geometrical parameters (i.e., buckling angle θ_0) and from Eq. (4), λ is expected to decrease with compressive strain in the $\hat{z}$ as f_2 is negative. We also want to note that there is no gauge field $\mathbf{A}_1$ since $\mathbf{k}$ is two dimensional, and thus M is not shifted. The changes in the Rashba dispersion and its locations due to out-of-plane strains are illustrated in Fig. 2(b). Notice that not including the angular dependence in the hopping correction will not capture this effect. The inclusion of the angular dependence is particularly important for the PbX monolayer due to its
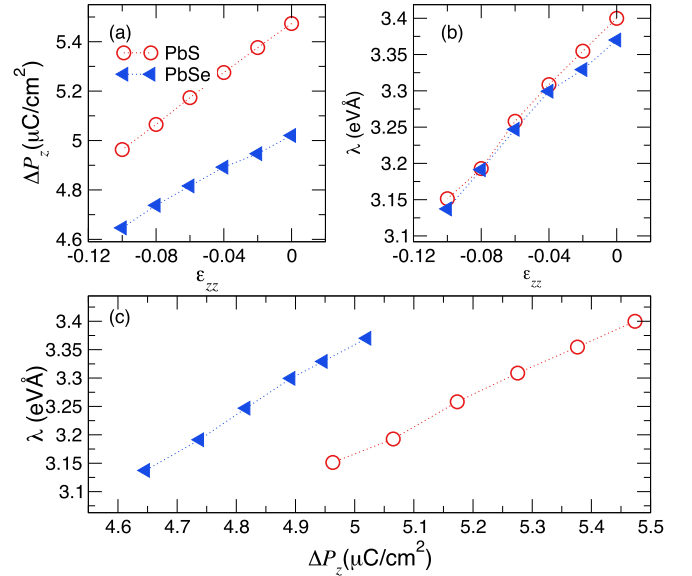

FIG. 3. (a) Out-of-plane polarization $\Delta\vec{\mathcal{P}}_z$ as a function of out-of-plane strain ϵ_{zz}. (b) Linear relationship between λ and ϵ_{zz} which is consistent with TB predictions. (c) Rashba parameter λ as a function of $\Delta\vec{\mathcal{P}}_z$. All data points are obtained from the DFT calculations.

buckled nature. Overall, this suggests that the out-of-plane internal electric polarization acts as an in-plane gauge field in the low-energy Hamiltonian. Assuming *small* strains, we found that $\lambda \propto |\vec{\mathcal{P}}_z|$. This result is important as it establishes a direct relationship between the Rashba field and the out-of-plane polarization, which is also proportional to the out-of-plane strain ϵ_{zz}. Recently, several works have also studied strain-induced piezoelectricity in boron nitride [40] and TMDCs [41]. Several experimental works use out-of-plane magnetic fields (parallel to the polar axis of Rashba materials) to measure the Rashba parameter as the Landau level spectrum changes with the strength of the Rashba parameter [14,42]. One could also use this experimental approach to detect variations in the Rashba parameter in PbX due to out-of-plane strains.

VI. CONCLUSIONS

We have developed a TB model where the electronic changes in PbX can be described within continuum mechanics. We found the scaling exponent that modifies the hopping parameter to be $\beta \simeq 3$. In the low-energy Hamiltonian, the effect of strains can be described as gauge fields, which are equivalent to, by minimal coupling, application of an in-plane magnetic field. Our theory describes how the location of the Rashba point and the strength of the Rashba field can be engineered by applying strains. The out-of-plane strain in particular is directly related to the out-of-plane polarization. Within this framework we are able to understand the connection between the Rashba and ferroelectricity.

Our strain-dependent TB model should be applicable for calculating the effects of inhomogeneous strain on the spatially resolved Rashba fields over a large region, whereas this calculation would not be feasible within a reasonable time using a DFT approach. Employing classical atomistic

simulations (e.g., molecular dynamics) together with strain-dependent TB will be an efficient tool for studying larger and more realistic systems with strain modulation due to substrates, indentors [12,13,43], or geometrical cuts [28,44]. This will open possibilities of using lead chalcogenides for strain and electric-controlled spintronic devices.

APPENDIX A: COMPUTATIONAL DETAILS

To validate our tight-binding predictions, we performed density functional theory (DFT) calculations implemented in the QUANTUM ESPRESSO package [45]. We employed projector augmented-wave (PAW) type pseudopotentials with Perdew-Burke-Ernzerhof (PBE) within the generalized gradient approximation (GGA) for the exchange and correlation functional with Ref. [46]. The Kohn-Sham orbitals were expanded in a plane-wave basis with a cutoff energy of 100 Ry and a charge density cutoff of 200 Ry. The cutoff was chosen following the suggested minimum cutoff in the pseudopotential file. A k-point grid sampling was generated using the Monkhorst-Pack scheme with $16 \times 16 \times 1$ points [47]. A vacuum of 20 Å was used. The relaxed structures of PbS, PbSe, and PbTe were obtained by relaxing the ionic positions and the lattice vectors. A convergence threshold on a total energy of 10^{-5} eV and a convergence threshold on forces of 0.005 eV/Å^{-1} were chosen. Lattice vectors are relaxed until the stress is less than 0.01 GPa. Our first-principles calculations show that the buckled phase of the PbX monolayer is more stable than the centrosymmetric planar phase [8], consistent with other DFT studies [16,48]. Detailed discussions on the bistable nature, ferroelectric properties, and orbital-spin texture properties of lead chalcogenides can be found in our previous paper [8]. In the current work, the deformations (atomic distortions) are applied to the optimized buckled structure.

We used a finer grid for band-structure calculations with the spin-orbit interaction included. We have tried several large numbers of k points and found that a grid of 100 k points between two symmetry points (e.g., between X and M) is enough to obtain the Rashba parameter λ at the M point [8]. A regular grid of $40 \times 40 \times 1$ was used for the surface plot of the energy spin splitting.

Here, we tabulate the optimized (relaxed) geometrical parameters of buckled PbX (X = S, Se, and Te) monolayers in Table I. The Rashba parameters λ are obtained by taking the derivative of energy dispersion near the M point. The orbital coefficients are obtained by projecting the wave functions into the atomic orbital basis. The unstrained values of λ and Δ are tabulated in Table II. From the table it can be seen that the wave

TABLE I. Relaxed lattice constant a, buckling angle θ, buckling height d_z, and nearest-neighbor bond distance d.

	a(Å)	θ (deg)	d_z(Å)	d(Å)
PbS	3.74	21.6	1.04	2.84
PbSe	3.82	24.3	1.22	2.96
PbTe	4.01	26.3	1.40	3.16

functions are mostly composed of in-plane and out-of-plane p orbitals of Pb and an in-plane orbital of the chalcogen X (X = S, Se, Te).

APPENDIX B: ELECTRIC POLARIZATION

We used the modern theory of polarization [38] to calculate the spontaneous polarization implemented in the QUANTUM ESPRESSO package [45]. The electric polarization is calculated via a Berry phase calculation [38], which is given by

$$\vec{\mathcal{P}} = \frac{1}{V} \sum_{\tau} q_\tau^{\text{ion}} \mathbf{R}_\tau - \frac{2i\text{e}}{(2\pi)^3} \sum_n^{\text{occ}} \int_{\text{BZ}} d^3\mathbf{k} e^{-i\vec{k}\cdot\mathbf{R}} \left\langle \Psi_{n\mathbf{k}} \left| \frac{\partial \Psi_{n\mathbf{k}}}{\partial \mathbf{k}} \right\rangle \right., \tag{B1}$$

where q_τ is the ionic charge plus the core electrons, $\mathbf{R}_\tau$ is the position of ions, V is the unit cell volume, e is the elementary charge, n is the valence band index, $\mathbf{k}$ is the wave vector, and $\Psi_{n\mathbf{k}}$ is the electronic wave function. The first term is the contribution from core electrons and ions, and the second term is the electronic contribution defined as the adiabatic flow of current which can be calculated from the Berry connection [38].

The spontaneous polarization is calculated by taking the difference between the polarization of the polar (buckled) state and the nonpolar (reference) state, $\Delta\vec{\mathcal{P}} = \vec{\mathcal{P}}_{\text{polar}} - \vec{\mathcal{P}}_{\text{nonpolar}}$. To find the polarization at different heights, we change the out-of-plane distance between the Pb and X (X = S, Se) atom while keeping the in-plane lattice vectors fixed at the optimized buckled values. It is a common practice to use a value on the order of the bulk lattice constant (0.5–1 nm) to estimate the monolayer thickness in order to compare the polarizations of the monolayers to the typical bulk ferroelectrics [49–51]. In this current work, we estimate the thickness to be 0.5 nm. In QUANTUM ESPRESSO, spontaneous polarization with the spin orbit included can be calculated using norm conserving pseudopotentials. A difference of 0.03 μC/cm^2 is found when the spin-orbit interaction is included. Thus, to save computational time, we only report spontaneous polarization without inclusion of the spin-orbit interaction. This small difference has also been reported previously [35,52]. In Fig. 4 we plot the

TABLE II. Rashba parameters λ, projected wave-function coefficients $|c_0|^2$, $|c_1|^2$, $|c_2|^2$ obtained from DFT, and Δ.

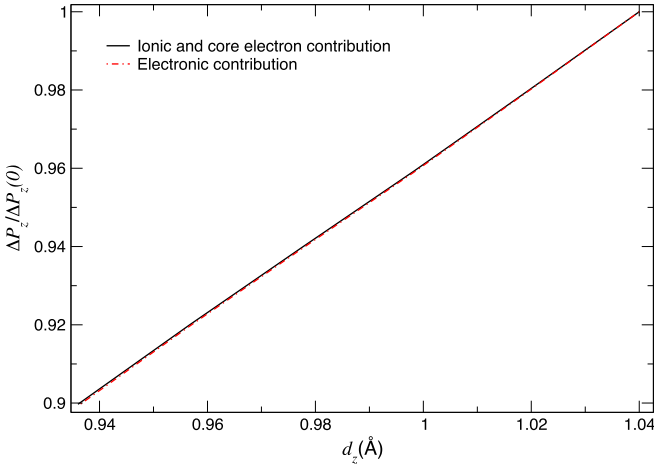|	$|c_0|^2$	$|c_1|^2$	$|c_2|^2$	λ (eV Å)	Δ (eV)
PbS	0.305	0.534	0.115	3.40	5.36
PbSe	0.272	0.549	0.137	3.37	4.28
PbTe	0.286	0.522	0.130	3.18	3.83

FIG. 4. From the DFT results we found that the ionic plus core electronic and the electronic (by a Berry phase calculation) contributions are proportional to the distance between Pb and X ($X =$ S, Se) in the z direction.

polarization from the ionic plus core electron contribution, and the electronic contribution, from the Berry phase calculation, scaled by their values at zero strain as a function of distance between the Pb and S atom in the z direction.

APPENDIX C: TIGHT BINDING

The lead chalcogenide monolayer has two atoms per unit cell (A, B). Based on density functional theories, the relevant orbitals near the valence and conduction bands are s and p orbitals. The wave function of sublattice A then can be written as

$$\psi^A(r) = \frac{1}{\sqrt{N}} \sum_{\mathbf{k},\mu} e^{i\mathbf{k}\cdot\mathbf{R}} a_{\mu,\mathbf{k}} \phi_\mu(\mathbf{r} - \mathbf{R}), \qquad (C1)$$

where $\mathbf{R}$ is the lattice vector, $\mathbf{k}$ is a wave vector, and μ is the basis wave function $[s, p_x, p_y, p_z]$. Including only nearest-neighbor hopping, the spinless Hamiltonian can be written as

$$H_{\text{orb}} = \sum_{\mu,\nu} \sum_{i,j} [t_{ij,\mu\nu} c^\dagger_{i,\mu} c_{j,\nu} + \text{H.c.}] + \sum_{\mu,\nu} \sum_i E_{\mu\nu} c^\dagger_{i,\mu} c_{i,\nu}, \qquad (C2)$$

where $\langle i, j \rangle$ runs over the on-site cell and the nearest-neighboring cells. $c^\dagger_{i,\mu}$ creates an electron in the unit cell i with atomic orbital μ. We can write this more compactly as

$$H_{\text{orb}} = \begin{pmatrix} H_{AA} & H_{AB} \\ H^\dagger_{AB} & H_{BB} \end{pmatrix}, \qquad (C3)$$

where H_{AA} (the on-site term) is given by

$$H_{AA} = \begin{pmatrix} E^s_A & 0 & 0 & 0 \\ 0 & E^{p_x}_A & 0 & 0 \\ 0 & 0 & E^{p_y}_A & 0 \\ 0 & 0 & 0 & E^{p_z}_A \end{pmatrix}. \qquad (C4)$$

To write down the hopping matrix, we use the following Slater-Koster matrix elements for the orbitals of neighboring atoms [20],

$$\begin{aligned} &s\text{-}s: V_{ss\sigma}, \\ &s\text{-}p: V_{sp\sigma}\hat{d}\cdot\hat{o}_j, \\ &p\text{-}p: (\hat{o}_i\cdot\hat{o}_j)V_{pp\pi} + (\hat{o}_i\cdot\hat{d})(\hat{o}_j\cdot\hat{d})(V_{pp\sigma} - V_{pp\pi}). \end{aligned} \qquad (C5)$$

Here, $\hat{o}_i$ is the orientation of the ith orbital and $\hat{d}$ is the unit vector pointing from atom 1 to atom 2. If we include up to first nearest neighbors only we can write the interlattice hopping matrix $H_{AB} \equiv K$ as

$$
\begin{aligned}
K = \Theta_\Gamma &\begin{pmatrix} V_{ss\sigma} & 0 & 0 & -\gamma V^{(1)}_{sp\sigma} \\ 0 & V_{pp\pi} + \alpha^2\Delta & 0 & 0 \\ 0 & 0 & V_{pp\pi} + \alpha^2\Delta & 0 \\ \gamma V^{(2)}_{sp\sigma} & 0 & 0 & V_{pp\pi} + \gamma^2\Delta \end{pmatrix} + 4\alpha^2\Delta\Theta_M \begin{pmatrix} 0 & 0 & 0 & 0 \\ 0 & 0 & 1 & 0 \\ 0 & 1 & 0 & 0 \\ 0 & 0 & 0 & 0 \end{pmatrix} \\
&+ 4\alpha\Theta_X \begin{pmatrix} 0 & iV^{(1)}_{sp\sigma} & 0 & 0 \\ -iV^{(2)}_{sp\sigma} & 0 & 0 & -i\gamma\Delta \\ 0 & 0 & 0 & 0 \\ 0 & -i\gamma\Delta & 0 & 0 \end{pmatrix} + 4\alpha\Theta_Y \begin{pmatrix} 0 & 0 & iV^{(1)}_{sp\sigma} & 0 \\ 0 & 0 & 0 & 0 \\ -iV^{(2)}_{sp\sigma} & 0 & 0 & -i\gamma\Delta \\ 0 & 0 & -i\gamma\Delta & 0 \end{pmatrix},
\end{aligned} \qquad (C6)
$$

where $\Theta_{\Gamma,M,X,Y} = [\cos\frac{k_x a}{2}\cos\frac{k_y a}{2}, \sin\frac{k_x a}{2}\sin\frac{k_y a}{2}, \sin\frac{k_x a}{2}\cos\frac{k_y a}{2}, \sin\frac{k_y a}{2}\cos\frac{k_x a}{2}]$. The momentum $\pi/a \leqslant k_{x/y} \leqslant \pi/a$ and $\gamma = \sin\theta$. To keep the expression more compact, we have introduced $\Delta = V_{pp\sigma} - V_{pp\pi}$. In addition, since the A and B species are not necessarily the same, we have two quantities of the $V_{sp\sigma}$ form.

While it is convenient to use s and p orbitals to write down the hopping matrix, since we are interested in including SOI in our model, it is helpful to go to a basis which is more natural for the angular momentum operators,

$$|0,0\rangle = |s\rangle, \quad |1,\pm1\rangle = \frac{\mp|p_x\rangle - i|p_y\rangle}{\sqrt{2}}, \quad |1,0\rangle = |p_z\rangle, \qquad (C7)$$

where the first number represents the orbital momentum quantum number and the second one is its projection along the $\hat{z}$ direction. This basis change does not alter the H_{AA} and H_{BB} matrices. The interlattice hopping portion of the Hamiltonian, on the other

hand, becomes

$$
\bar{K} = \Theta_\Gamma \underbrace{\begin{pmatrix} V_{ss\sigma} & 0 & 0 & -\gamma V_{sp\sigma}^{(1)} \\ 0 & V_{pp\pi} + \alpha^2\Delta & 0 & 0 \\ 0 & 0 & V_{pp\pi} + \alpha^2\Delta & 0 \\ \gamma V_{sp\sigma}^{(2)} & 0 & 0 & V_{pp\pi} + \gamma^2\Delta \end{pmatrix}}_{K_\Gamma} + 4\alpha^2\Delta\Theta_M \underbrace{\begin{pmatrix} 0 & 0 & 0 & 0 \\ 0 & 0 & -i & 0 \\ 0 & i & 0 & 0 \\ 0 & 0 & 0 & 0 \end{pmatrix}}_{K_M}
$$

$$
+ 2\sqrt{2}\alpha\Theta_X \underbrace{\begin{pmatrix} 0 & -iV_{sp\sigma}^{(1)} & iV_{sp\sigma}^{(1)} & 0 \\ iV_{sp\sigma}^{(2)} & 0 & 0 & i\gamma\Delta \\ -iV_{sp\sigma}^{(2)} & 0 & 0 & -i\gamma\Delta \\ 0 & i\gamma\Delta & -i\gamma\Delta & 0 \end{pmatrix}}_{K_X} + 2\sqrt{2}\alpha\Theta_Y \underbrace{\begin{pmatrix} 0 & V_{sp\sigma}^{(1)} & V_{sp\sigma}^{(1)} & 0 \\ V_{sp\sigma}^{(2)} & 0 & 0 & \gamma\Delta \\ V_{sp\sigma}^{(2)} & 0 & 0 & \gamma\Delta \\ 0 & -\gamma\Delta & -\gamma\Delta & 0 \end{pmatrix}}_{K_Y}. \tag{C8}
$$

From here we write $H \equiv U H_{\text{orb}} U^{-1}$, where U is a matrix projector from the orbital basis to the angular momentum basis. To include the SOI, we use the standard form describing the spin-orbit coupling arising from the interaction with the nucleus,

$$
H_{\text{SOI}} = T_{\mathcal{X}} \left(\frac{L_+ \otimes s_- + L_- \otimes s_+}{2} + L_z \otimes s_z \right), \tag{C9}
$$

where $\mathcal{X}$ is either Pb or X ($X = $ S, Se, Te). The last term modifies the diagonal elements of the self-energy for $|1,\pm1\rangle$ by adding (subtracting) $T_X/2$ if L_z and s_z point in the same (opposite) direction. The first term couples $|1,1\rangle \otimes |\downarrow\rangle$ with $|1,0\rangle \otimes |\uparrow\rangle$ and $|1,-1\rangle \otimes |\uparrow\rangle$ with $|1,0\rangle \otimes |\downarrow\rangle$ with the coupling strength $T_X/\sqrt{2}$.

The total Hamiltonian can then be written as

$$
H_{\text{tot}} = H \otimes 1_{2x2} + H_{\text{SOI}}. \tag{C10}
$$

M point

We first look around the M point $k_x = k_y = \pi/a$. To the leading order in q, the hopping matrix $\tilde{K}$ is given by

$$
\tilde{K} = 4\alpha^2\Delta \begin{pmatrix} 0 & 0 & 0 & 0 \\ 0 & 0 & -i & 0 \\ 0 & i & 0 & 0 \\ 0 & 0 & 0 & 0 \end{pmatrix} - a\sqrt{2}\alpha q \begin{pmatrix} 0 & V_{sp\sigma}^{(1)} e^{-i\phi} & V_{sp\sigma}^{(1)} e^{i\phi} & 0 \\ V_{sp\sigma}^{(2)} e^{i\phi} & 0 & 0 & \gamma\Delta e^{i\phi} \\ V_{sp\sigma}^{(2)} e^{-i\phi} & 0 & 0 & \gamma\Delta e^{-i\phi} \\ 0 & -\gamma\Delta e^{-i\phi} & -\gamma\Delta e^{i\phi} & 0 \end{pmatrix}, \tag{C11}
$$

where ϕ is the angle measured from the $\hat{x}$ direction. At $q = 0$ ($k_x = k_y = \pi/a$), the Hamiltonian decomposes into several uncoupled blocks with the corresponding bases,

$$
H_s^{m,\pm} = E_m^s : |0,0\rangle \otimes |\pm\rangle \otimes |m\rangle, \quad H_p^{mn,\pm} = \begin{pmatrix} E_m^p - \frac{T_m}{2} & \frac{T_m}{\sqrt{2}} & \mp4i\alpha^2\Delta \\ \frac{T_m}{\sqrt{2}} & E_m^p & 0 \\ \pm4i\alpha^2\Delta & 0 & E_n^p + \frac{T_n}{2} \end{pmatrix} : \begin{pmatrix} |m\rangle \otimes |1,\pm1\rangle \otimes |\mp\rangle \\ |m\rangle \otimes |1,0\rangle \otimes |\pm\rangle \\ |n\rangle \otimes |1,\mp1\rangle \otimes |\mp\rangle \end{pmatrix}, \tag{C12}
$$

where $m \neq n$ labels the sublattices and the middle $|\pm\rangle$ ket denotes the spin state. Using the direct sum notation, we can write down the total Hamiltonian as $H = H_s^{A,+} \oplus H_s^{A,-} \oplus H_s^{B,+} \oplus H_s^{B,-} \oplus H_p^{AB,+} \oplus H_p^{AB,-} \oplus H_p^{BA,+} \oplus H_p^{BA,-}$.

From H_s, we see that for a given m, the eigenstates are spin degenerate. The degeneracy becomes fourfold if the atoms of sublattices A and B are the same, leading to $E_A^p = E_B^p$. Equation (C11) shows that at finite q there is no coupling between the degenerate $|0,0\rangle$ states that is linear in the momentum. This means that the bands composed of s orbitals have local extrema at the M point.

Next, we turn to H_p from Eq. (C12). Just as for H_s, the bands are doubly or fourfold degenerate depending on whether the sublattices are composed of the same atomic species. Without making assumptions about the lattice composition, the general form of the degenerate states is

$$
|\Psi^\pm\rangle_{mn} = c_0|m\rangle \otimes |1,\pm1\rangle \otimes |\mp\rangle + c_1|m\rangle \otimes |1,0\rangle \otimes |\pm\rangle \pm ic_2|n\rangle \otimes |1,\mp1\rangle \otimes |\mp\rangle, \tag{C13}
$$

with c_0, c_1, and c_2 real. At finite q,

$$
{}_{mn}\langle\Psi^+|H|\Psi^-\rangle_{mn} = -a\sin2\theta c_1 c_2 (\Delta iq e^{-i\phi})\varepsilon_{mn}, \tag{C14}
$$

where $\varepsilon_{AB} = -\varepsilon_{BA} = 1$ is the two-dimensional Levi-Civita symbol. This coupling between the degenerate states leads to an effective Rashba-like Hamiltonian,

$$
H_{\text{eff}}^{mn} = a\sin2\theta c_1 c_2 \Delta\varepsilon_{mn}[(\mathbf{q}\times\boldsymbol{\sigma})\cdot\hat{z}] : \begin{pmatrix} |\Psi^+\rangle_{mn} \\ |\Psi^-\rangle_{mn} \end{pmatrix}, \tag{C15}
$$

or in the matrix form,

$$H_{\text{eff}} = \begin{pmatrix} 0 & -i\lambda(q_x - iq_y) \\ i\lambda(q_x + iq_y) & 0 \end{pmatrix}. \tag{C16}$$

We use values of c_0, c_1, and c_2 obtained from DFT results. To give better physical pictures of these coefficients, we will solve the Hamiltonian Eq. (C12). We treat the spin-orbit interaction (SOI) as perturbations and we will assume that $T_m \gg T_n$, where m is the index denoting Pb with strong SOI and n denotes weak SOI of the chalcogen atom. Focusing on $H_p^{mn,+}$, Eq. (C12) becomes

$$H_p^{mn,+} = \begin{pmatrix} E_m^p & 0 & -4i\alpha^2\Delta \\ 0 & E_m^p & 0 \\ 4i\alpha^2\Delta & 0 & E_n^p \end{pmatrix} : \begin{pmatrix} |m\rangle \otimes |1,1\rangle \otimes |-\rangle \\ |m\rangle \otimes |1,0\rangle \otimes |+\rangle \\ |n\rangle \otimes |1,-1\rangle \otimes |-\rangle \end{pmatrix}, \tag{C17}$$

and the perturbation

$$\delta H_p^{mn,+} = \begin{pmatrix} -\frac{T_m}{2} & \frac{T_m}{\sqrt{2}} & 0 \\ \frac{T_m}{\sqrt{2}} & 0 & 0 \\ 0 & 0 & 0 \end{pmatrix} : \begin{pmatrix} |m\rangle \otimes |1,1\rangle \otimes |-\rangle \\ |m\rangle \otimes |1,0\rangle \otimes |+\rangle \\ |n\rangle \otimes |1,-1\rangle \otimes |-\rangle \end{pmatrix}. \tag{C18}$$

We first solved Eq. (C17) to find the eigenvalues and eigenvectors and used first-order perturbation theory to obtain the corrections to the eigenvectors. Using MATHEMATICA, we found to the first order in T_m that

$$|c_1 c_2| \simeq \frac{T_m\left(E_m^p - E_n^p + \sqrt{\left(E_m^p - E_n^p\right)^2 + 64\alpha^4\Delta^2}\right)}{8\sqrt{2}\alpha^2\Delta\left(E_n^p - E_m^p + \sqrt{\left(E_m^p - E_n^p\right)^2 + 64\alpha^4\Delta^2}\right)}. \tag{C19}$$

Recall that we defined the Rashba parameter $\lambda \equiv a \sin 2\theta \Delta c_1 c_2$. From Eq. (C19) we see that $|c_1 c_2|$ weakly depends on strains. For this reason, in the main text we assumed c_1 and c_2 are constant and the corrections to λ come mostly from Δ and θ.

APPENDIX D: MAGNETIC FIELD

Let us now try to include external fields to the system. The magnetic field can be included via the Peierls substitution so that $\mathbf{q} \to \mathbf{q} - e\mathbf{A}/c$, where $\mathbf{A}$ is the vector potential. In addition, applying an external magnetic field leads to the interaction of the electron angular momentum with the field.

The total magnetic moment of an electron is given by

$$\mu = -\mu_B \frac{\mathbf{L} + 2\mathbf{S}}{\hbar}, \tag{D1}$$

so that

$$\mathbf{B} \cdot \mu = -\mu_B \frac{B_x\left(\frac{L_+ + L_-}{2} + S_+ + S_-\right) + B_y\left(\frac{L_+ - L_-}{2i} + \frac{S_+ - S_-}{i}\right) + B_z(L_z + 2S_z)}{\hbar}. \tag{D2}$$

Setting $\mathbf{B} = (B_\parallel \cos\tau, B_\parallel \sin\tau, B_\perp)$ gives

$$\mathbf{B} \cdot \mu = -\mu_B \frac{B_\parallel \cos\tau\left(\frac{L_+ + L_-}{2} + S_+ + S_-\right) - iB_\parallel \sin\tau\left(\frac{L_+ - L_-}{2} + S_+ - S_-\right) + B_\perp(L_z + 2S_z)}{\hbar}$$

$$= -\mu_B \frac{B_\parallel\left[e^{-i\tau}\left(\frac{L_+}{2} + S_+\right) + e^{i\tau}\left(\frac{L_-}{2} + S_-\right)\right] + B_\perp(L_z + 2S_z)}{\hbar}. \tag{D3}$$

The first term $\propto B_\parallel$ introduces coupling between $|\Psi^\pm\rangle$ while the last term $\propto B_\perp$ modifies and breaks the symmetry between the degenerate states. Starting with last term, we get

$$\langle\Psi^+|\mathbf{B} \cdot \mu|\Psi^+\rangle = -\langle\Psi^-|\mathbf{B} \cdot \mu|\Psi^-\rangle = -\mu_B B_\perp\left(c_1^2 - 2c_2^2\right). \tag{D4}$$

Next, we apply the first term onto $|\Psi^+\rangle$,

$$-\mu_B \frac{B_\parallel\left[e^{-i\tau}\left(\frac{L_+}{2} + S_+\right) + e^{i\tau}\left(\frac{L_-}{2} + S_-\right)\right]}{\hbar}(c_0|m\rangle \otimes |1,1\rangle \otimes |-\rangle + c_1|m\rangle \otimes |1,0\rangle \otimes |+\rangle + ic_2|n\rangle \otimes |1,-1\rangle \otimes |-\rangle)$$

$$= -\mu_B B_\parallel\left[e^{-i\tau}c_0|m\rangle|1,1\rangle|+\rangle + e^{-i\tau}\frac{c_0}{\sqrt{2}}|m\rangle|1,0\rangle|-\rangle + e^{-i\tau}\frac{c_1}{\sqrt{2}}|m\rangle|1,1\rangle|+\rangle\right.$$

$$\left. + e^{i\tau}\frac{c_1}{\sqrt{2}}|m\rangle|1,-1\rangle|+\rangle + e^{i\tau}c_1|m\rangle|1,0\rangle|-\rangle + e^{-i\tau}i\frac{c_2}{\sqrt{2}}|n\rangle|1,0\rangle|-\rangle + e^{i\tau}ic_2|n\rangle|1,-1\rangle|+\rangle\right]$$

$$= -\mu_B B_\parallel \left[e^{i\tau} \left(\frac{c_0}{\sqrt{2}} + c_1 \right) |m\rangle|1,0\rangle|-\rangle + e^{-i\tau} \left(c_0 + \frac{c_1}{\sqrt{2}} \right) |m\rangle|1,1\rangle|+\rangle + c_1 e^{i\tau} c_1 |m\rangle|1,-1\rangle|+\rangle \right.$$
$$\left. + e^{-i\tau} i \frac{c_2}{\sqrt{2}} |n\rangle|1,0\rangle|-\rangle + e^{i\tau} i c_2 |m\rangle|1,-1\rangle|+\rangle \right]. \tag{D5}$$

Now, we apply $\langle \Psi^- |$ onto Eq. (D5). We see that the states on $|n\rangle$ drop out. The remaining states yield

$$\langle \Psi^- | \mathbf{B} \cdot \mu | \Psi^+ \rangle = -\mu_B B_\parallel e^{i\tau} \left[c_1 \left(\frac{c_0}{\sqrt{2}} + c_1 + c_0 \right) \right]. \tag{D6}$$

Thus, our general Hamiltonian becomes

$$H = \lambda \left[\left(\mathbf{q} - \frac{e\mathbf{A}}{c} \right) \times \boldsymbol{\sigma} \right] \cdot \hat{z} + m_\perp \sigma_z B_\perp + m_\parallel \mathbf{B}_\parallel \cdot \sigma_\parallel, \tag{D7}$$

where $m_\perp = -\mu_B(c_1^2 - 2c_2^2)$ and $m_\parallel = -\mu_B[c_1(\frac{c_0}{\sqrt{2}} + c_1 + c_0)]$.

APPENDIX E: IN-PLANE FIELD

If the field is in plane, the Hamiltonian is given by

$$H = \begin{pmatrix} 0 & i\lambda q e^{i\phi} + \mathcal{B} e^{-i\tau} \\ -i\lambda q e^{-i\phi} + \mathcal{B} e^{i\tau} & 0 \end{pmatrix} = \lambda \begin{pmatrix} 0 & iq e^{i\phi} + \frac{\mathcal{B}}{\lambda} e^{-i\tau} \\ -iq e^{-i\phi} + \frac{\mathcal{B}}{\lambda} e^{i\tau} & 0 \end{pmatrix}, \tag{E1}$$

where we have defined $\mathcal{B} \equiv m_\parallel B_\parallel$. The eigenvalues become

$$\mathcal{E} = \pm \lambda \sqrt{ \left(q_x - \frac{\mathcal{B}}{\lambda} \sin \tau \right)^2 + \left(q_y - \frac{\mathcal{B}}{\lambda} \cos \tau \right)^2 }. \tag{E2}$$

Applying an in-plane magnetic field shifts the cone in the Brillouin zone.

Let us take a closer look at the Hamiltonian,

$$H = \lambda \begin{pmatrix} 0 & i\left[\left(q_x - \frac{\mathcal{B}}{\lambda} \sin \tau \right) + i\left(q_y - \frac{\mathcal{B}}{\lambda} \cos \tau \right) \right] \\ -i\left[\left(q_x - \frac{\mathcal{B}}{\lambda} \sin \tau \right) - i\left(q_y - \frac{\mathcal{B}}{\lambda} \cos \tau \right) \right] & 0 \end{pmatrix} = \lambda \begin{pmatrix} 0 & ip e^{i\xi} \\ -ip e^{-i\xi} & 0 \end{pmatrix}. \tag{E3}$$

The eigenstates are

$$|I\rangle = \frac{|\Psi^+\rangle + i e^{-i\xi} |\Psi^-\rangle}{\sqrt{2}}, \quad |II\rangle = \frac{|\Psi^+\rangle - i e^{-i\xi} |\Psi^-\rangle}{\sqrt{2}}. \tag{E4}$$

Now we can obtain the in-plane spin texture for the cones. First, it is easy to show that

$$\langle \Psi^I | \sigma_{x/y} | \Psi^I \rangle = \langle \Psi^{II} | \sigma_{x/y} | \Psi^{II} \rangle = 0. \tag{E5}$$

Next,

$$\langle \Psi^{II} | \sigma_x | \Psi^I \rangle = c_1^2 \langle + | \sigma_x | - \rangle = c_1^2, \quad \langle \Psi^{II} | \sigma_y | \Psi^I \rangle = c_1^2 \langle + | \sigma_y | - \rangle = -i c_1^2. \tag{E6}$$

This leads to

$$\langle I | \sigma_x | I \rangle = \frac{-i e^{i\xi}}{2} c_1^2 + \frac{i e^{-i\xi}}{2} c_1^2 = -i \frac{c_1^2}{2} (e^{i\xi} - e^{-i\xi}) = c_1^2 \sin \xi,$$

$$\langle I | \sigma_y | I \rangle = -i c_1^2 \frac{-i e^{i\xi}}{2} + i c_1^2 \frac{i e^{-i\xi}}{2} = -c_1^2 \frac{e^{i\xi}}{2} - c_1^2 \frac{e^{-i\xi}}{2} = -c_1^2 \cos \xi,$$

$$\langle II | \sigma_x | II \rangle = \frac{i e^{i\xi}}{2} c_1^2 + \frac{-i e^{-i\xi}}{2} c_1^2 = -c_1^2 \sin \xi,$$

$$\langle II | \sigma_y | II \rangle = i c_1^2 \frac{-i e^{i\xi}}{2} - i c_1^2 \frac{i e^{-i\xi}}{2} = c_1^2 \cos \xi. \tag{E7}$$

As a result, the spin texture becomes

$$\langle I | \hat{\sigma} | I \rangle = c_1^2 (\hat{x} \sin \xi - \hat{y} \cos \xi) \propto (\hat{x} p_y - \hat{y} p_x), \quad \langle II | \hat{\sigma} | II \rangle = -c_1^2 (\hat{x} \sin \xi - \hat{y} \cos \xi) \propto -(\hat{x} p_y - \hat{y} p_x). \tag{E8}$$

Recall that

$$p_x = q_x - \frac{\lambda}{\hbar v} \sin \tau, \quad p_y = q_y - \frac{\lambda}{\hbar v} \cos \tau. \tag{E9}$$

This means that spin contours now revolve not around the $\mathbf{q} = \mathbf{0}$ point but instead around a $\mathbf{p} = \mathbf{0}$ point.

[1] A. K. Geim and I. V. Grigorieva, Nature (London) **499**, 419 (2013).

[2] K. Novoselov, A. Mishchenko, A. Carvalho, and A. C. Neto, Science **353**, aac9439 (2016).

[3] A. Manchon, H. C. Koo, J. Nitta, S. Frolov, and R. Duine, Nat. Mater. **14**, 871 (2015).

[4] J. D. Sau, R. M. Lutchyn, S. Tewari, and S. Das Sarma, Phys. Rev. Lett. **104**, 040502 (2010).

[5] L. Fu and C. L. Kane, Phys. Rev. Lett. **100**, 096407 (2008).

[6] K. Chang, J. Liu, H. Lin, N. Wang, K. Zhao, A. Zhang, F. Jin, Y. Zhong, X. Hu, W. Duan, Q. Zhang, L. Fu, Q.-K. Xue, X. Chen, and S.-H. Ji, Science **353**, 274 (2016).

[7] M. M. R. Moayed, T. Bielewicz, M. S. Zöllner, C. Herrmann, and C. Klinke, Nat. Commun. **8**, 15721 (2017).

[8] P. Z. Hanakata, A. S. Rodin, A. Carvalho, H. S. Park, D. K. Campbell, and A. H. Castro Neto, Phys. Rev. B **96**, 161401 (2017).

[9] D. Di Sante, P. Barone, R. Bertacco, and S. Picozzi, Adv. Mater. **25**, 509 (2013).

[10] D. Di Sante, A. Stroppa, P. Barone, M.-H. Whangbo, and S. Picozzi, Phys. Rev. B **91**, 161401 (2015).

[11] C. Rinaldi, S. Varotto, M. Asa, J. Sławińska, J. Fujii, G. Vinai, S. Cecchi, D. Di Sante, R. Calarco, I. Vobornik, G. Panaccione, S. Picozzi, and R. Bertacco, Nano Lett. **18**, 2751 (2018).

[12] N. Levy, S. Burke, K. Meaker, M. Panlasigui, A. Zettl, F. Guinea, A. C. Neto, and M. Crommie, Science **329**, 544 (2010).

[13] A. Castellanos-Gomez, R. Roldán, E. Cappelluti, M. Buscema, F. Guinea, H. S. van der Zant, and G. A. Steele, Nano Lett. **13**, 5361 (2013).

[14] J. R. Bindel, M. Pezzotta, J. Ulrich, M. Liebmann, E. Y. Sherman, and M. Morgenstern, Nat. Phys. **12**, 920 (2016).

[15] J. Liu, X. Qian, and L. Fu, Nano Lett. **15**, 2657 (2015).

[16] W. Wan, Y. Yao, L. Sun, C.-C. Liu, and F. Zhang, Adv. Mater. **29**, 1604788 (2017).

[17] A. S. Rodin, P. Z. Hanakata, A. Carvalho, H. S. Park, D. K. Campbell, and A. H. Castro Neto, Phys. Rev. B **96**, 115450 (2017).

[18] E. Tang and L. Fu, Nat. Phys. **10**, 964 (2014).

[19] P. Barone, D. Di Sante, and S. Picozzi, Phys. Status Solidi RRL **7**, 1102 (2013).

[20] J. C. Slater and G. F. Koster, Phys. Rev. **94**, 1498 (1954).

[21] W. A. Harrison, *Elementary Electronic Structure: Revised* (World Scientific, Singapore, 2004).

[22] M. A. Cazalilla, H. Ochoa, and F. Guinea, Phys. Rev. Lett. **113**, 077201 (2014).

[23] H. Rostami, R. Roldán, E. Cappelluti, R. Asgari, and F. Guinea, Phys. Rev. B **92**, 195402 (2015).

[24] S. Fang, S. Carr, J. Shen, M. A. Cazalilla, and E. Kaxiras, arXiv:1709.07510.

[25] J.-W. Jiang and H. S. Park, Phys. Rev. B **91**, 235118 (2015).

[26] E. Taghizadeh Sisakht, F. Fazileh, M. H. Zare, M. Zarenia, and F. M. Peeters, Phys. Rev. B **94**, 085417 (2016).

[27] Z. Qi, A. L. Kitt, H. S. Park, V. M. Pereira, D. K. Campbell, and A. H. Castro Neto, Phys. Rev. B **90**, 125419 (2014).

[28] Z. Qi, D. K. Campbell, and H. S. Park, Phys. Rev. B **90**, 245437 (2014).

[29] F. Guinea, M. Katsnelson, and A. Geim, Nat. Phys. **6**, 30 (2010).

[30] J. L. Mañes, F. de Juan, M. Sturla, and M. A. H. Vozmediano, Phys. Rev. B **88**, 155405 (2013).

[31] M. R. Masir, D. Moldovan, and F. Peeters, Solid State Commun. **175**, 76 (2013).

[32] F. de Juan, M. Sturla, and M. A. H. Vozmediano, Phys. Rev. Lett. **108**, 227205 (2012).

[33] A. L. Kitt, V. M. Pereira, A. K. Swan, and B. B. Goldberg, Phys. Rev. B **85**, 115432 (2012).

[34] M. Liebmann, C. Rinaldi, D. Di Sante, J. Kellner, C. Pauly, R. N. Wang, J. E. Boschker, A. Giussani, S. Bertoli, M. Cantoni, L. Baldrati, M. Asa, I. Vobornik, G. Panaccione, D. Marchenko, J. Sánchez-Barriga, O. Rader, R. Calarco, S. Picozzi, R. Bertacco, and M. Morgenstern, Adv. Mater. **28**, 560 (2016).

[35] L. Leppert, S. E. Reyes-Lillo, and J. B. Neaton, J. Phys. Chem. Lett. **7**, 3683 (2016).

[36] Q. Liu, Y. Guo, and A. J. Freeman, Nano Lett. **13**, 5264 (2013).

[37] X. Qian, L. Fu, and J. Li, Nano Res. **8**, 967 (2015).

[38] R. D. King-Smith and D. Vanderbilt, Phys. Rev. B **47**, 1651 (1993).

[39] A. Filippetti, V. Fiorentini, F. Ricci, P. Delugas, and J. Íñiguez, Nat. Commun. **7**, 11211 (2016).

[40] M. Droth, G. Burkard, and V. M. Pereira, Phys. Rev. B **94**, 075404 (2016).

[41] H. Rostami, F. Guinea, M. Polini, and R. Roldán, npj 2D Mater. Appl. **2**, 15 (2018).

[42] S. Bordács, J. G. Checkelsky, H. Murakawa, H. Y. Hwang, and Y. Tokura, Phys. Rev. Lett. **111**, 166403 (2013).

[43] A. Georgi, P. Nemes-Incze, R. Carrillo-Bastos, D. Faria, S. Viola Kusminskiy, D. Zhai, M. Schneider, D. Subramaniam, T. Mashoff, N. M. Freitag, M. Liebmann, M. Pratzer, L. Wirtz, C. R. Woods, R. V. Gorbachev, Y. Cao, K. S. Novoselov, N. Sandler, and M. Morgenstern, Nano Lett. **17**, 2240 (2017).

[44] P. Z. Hanakata, Z. Qi, D. K. Campbell, and H. S. Park, Nanoscale **8**, 458 (2016).

[45] P. Giannozzi, S. Baroni, N. Bonini, M. Calandra, R. Car, C. Cavazzoni, D. Ceresoli, G. L. Chiarotti, M. Cococcioni, I. Dabo, A. Dal Corso, S. de Gironcoli, S. Fabris, G. Fratesi, R. Gebauer, U. Gerstmann, C. Gougoussis, A. Kokalj, M. Lazzeri, L. Martin-Samos *et al.*, J. Phys.: Condens. Matter **21**, 395502 (19pp) (2009).

[46] J. P. Perdew, K. Burke, and M. Ernzerhof, Phys. Rev. Lett. **77**, 3865 (1996).

[47] H. J. Monkhorst and J. D. Pack, Phys. Rev. B **13**, 5188 (1976).

[48] K. Kobayashi, Surf. Sci. **639**, 54 (2015).

[49] P. Z. Hanakata, A. Carvalho, D. K. Campbell, and H. S. Park, Phys. Rev. B **94**, 035304 (2016).

[50] R. Fei, W. Kang, and L. Yang, Phys. Rev. Lett. **117**, 097601 (2016).

[51] H. Wang and X. Qian, 2D Mater. **4**, 015042 (2017).

[52] A. Stroppa, C. Quarti, F. De Angelis, and S. Picozzi, J. Phys. Chem. Lett. **6**, 2223 (2015).